International Journal of Multiphase Flow 122 (2020) 103155

Contents lists available at ScienceDirect

International Journal of Multiphase Flow

journal homepage: www.elsevier.com/locate/ijmulflow

Numerical investigation of partial cavitation regimes over a wedge using large eddy simulation

Mrugank Bhatt, Krishnan Mahesh*

Department of Aerospace Engineering and Mechanics, University of Minnesota, Minneapolis, MN 55455, USA

ARTICLE INFO

Article history:
Received 9 August 2019
Revised 24 October 2019
Accepted 30 October 2019
Available online 7 November 2019

Keywords:
Large eddy simulation (LES)
Sheet/cloud cavitation
Re-entrant jet
Bubbly shock waves
Partial cavitation

ABSTRACT

Partial cavitation over incipient, transitory and periodic regimes is investigated using large eddy simulation (LES) in the (experimental) sharp wedge configuration of Ganesh et al. (2016). The numerical approach is based on a compressible homogeneous mixture model with finite rate mass transfer between the phases. Physical mechanisms of cavity transition observed in the experiments; i.e. re-entrant jet and bubbly shock wave, are both captured in the LES over their respective regimes. Vapor volume fraction data obtained from the LES is quantitatively compared to X-ray densitometry. In the transitory and periodic regimes, void fractions resulting from complex interactions of large regions of vapor in the sheet/cloud show very good comparison with the experiments. In addition, very good agreement with the experiments is obtained for the shedding frequency and the bubbly shock wave propagation speed. In the incipient regime, the qualitative characteristics of the flow (e.g. cavitation inside spanwise vortices in the shear layer) are captured in the simulations. Conditions favoring either the formation of the re-entrant jet or the bubbly shock wave are analyzed by contrasting the LES results between the regimes. In the transitory regime, large pressure recovery from within the cavity to outside, and the resulting high adverse pressure gradient at the cavity closure support the formation of re-entrant jet. In the periodic regime, overall low pressures lead to reduced speed of sound and increased medium compressibility, favoring the propagation of shock waves. In a re-entrant jet cycle, vapor production occurs predominantly in the shear layer, and intermittently within the cavity. In a bubbly shock cycle, vapor production is observed spanning the entire thickness of the cavity. Bubbly shock wave propagation is observed to be initiated by the impingement of the collapse-induced pressure waves from the previously shed cloud. Supersonic Mach numbers are observed in the cavity closure regions, while the regions within the grown cavity are subsonic due to the negligible flow velocities.

1. Introduction

Cavitation is the phase change of liquid into vapor when the liquid pressure drops below vapor pressure. It is often encountered in hydrodynamic applications such as marine propulsors, hydrofoils, rotating turbomachinery etc., and exists over different regimes ranging from inception to massive regions of vapor. Cavitation is termed as 'partial cavitation' when the cavity closes on the cavitating surface. Ganesh et al. (2016) characterized partial cavitation over a wedge into incipient, transitory and periodic regimes. A schematic summarizing the characteristics of the regimes is shown in Fig. 1. Incipient cavitation is observed in the separated shear layers and often inside the low pressure cores of coherent vortices. With further reduction in cavitation number ($\sigma = 2(p - p_v)/(\rho u^2)$, where p_v is the vapor pressure), a sheet cavity forms over the wedge and intermittently sheds as a cloud (referred to as "sheet to cloud" transition) due to formation of a re-entrant jet at the cavity closure. This regime is referred to as the transitory regime. As σ is reduced further, the cavity periodically transitions from sheet to cloud due to the propagation of bubbly shock waves. This regime is termed as the periodic regime. In the present work, we analyze the performance of LES in capturing the physical characteristics of the regimes discussed by Ganesh et al. (2016). The numerical results are used to comment on the differences in the flow field that lead to the formation of either the re-entrant jet or bubbly shock waves. Some of these differences are highlighted in Fig. 1; e.g. streamline curvature, vapor production and collapse-induced pressure waves.

The role of liquid re-entrant jets in sheet to cloud transition has been investigated by various experimental and computational studies (Knapp, 1955; Kawanami et al., 1997; Arndt

* Corresponding author.
E-mail address: mahesh@aem.umn.edu (K. Mahesh).

https://doi.org/10.1016/j.ijmultiphaseflow.2019.103155
0301-9322/

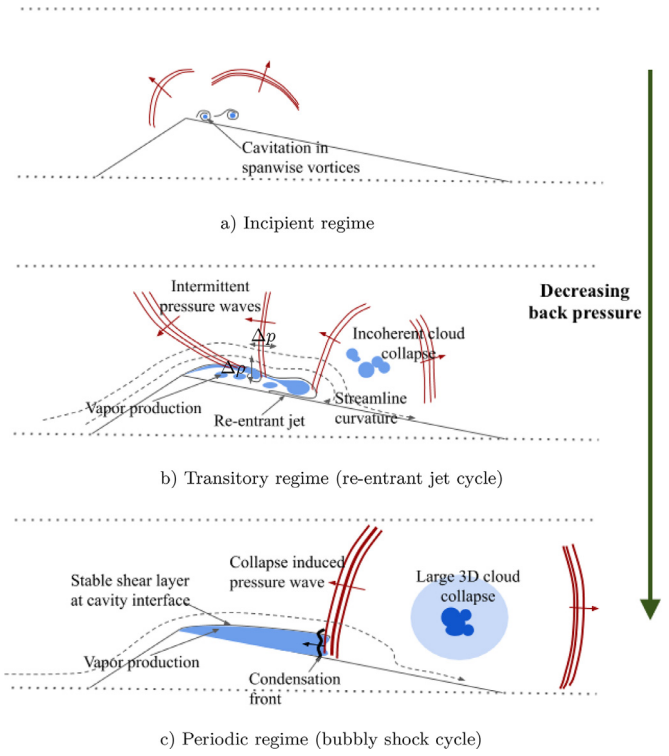

Fig. 1. Schematic summarizing the continuum over the partial cavitation regimes: a) incipient, b) transitory and c) periodic. Cavity interface is indicated by the solid black line, vapor regions are shown by blue, pressure waves are shown using red lines and streamlines are shown using dashed line followed by an arrow. Note that this is an overall depiction of the regimes and does not necessarily indicate the same instance of time. (For interpretation of the references to colour in this figure legend, the reader is referred to the web version of this article.)

et al., 2000; Gopalan and Katz, 2000; Callenaere et al., 2001; Laberteaux and Ceccio, 2001; Foeth et al., 2008; Frikha et al., 2008; Gnanaskandan and Mahesh, 2016b; Peng et al., 2016). Callenaere et al. (2001) showed that if the adverse pressure gradient at cavity closure is high enough, a re-entrant jet will develop. They observed two different cavity patterns based on the thickness of the cavity. For thick cavities, interaction of the re-entrant jet with the cavity is minimal leading to the classical sheet to cloud transition. For thin cavities, re-entrant jet propagation splits the cavity into many small structures. The thin cavity appears rather like a two-phase mixture of approximately constant length. Laberteaux and Ceccio (2001) further classified cavities as 'open' or 'closed' based on the absence or presence of re-entrant jet, in their experimental study over a wedge. They described an open cavity as typically frothy without a clear re-entrant jet, while a closed cavity had a sharp interface and exhibited cloud shedding due to re-entrant jet formation. They observed that the flow around the closed cavity was largely irrotational. Gopalan and Katz (2000) using particle image velocimetry (PIV) and high speed videography studied the flow structures in the cavity closure region. They observed that the process of cavity collapse involves roll up of large hairpin-like vortices and substantial vorticity production. In addition, both Laberteaux and Ceccio (2001) and Gopalan and Katz (2000) concluded that the adverse pressure gradient is necessary for the formation of re-entrant jet, in line with Callenaere et al. (2001).

It is known that the sound speed of the two-phase mixture is orders of magnitude smaller than its constituent phases (Franc and Michel, 2005). Hence, regions in the bubbly mixture are susceptible to the formation of shock waves if the sound speed becomes comparable to the flow velocities. Appearance of shock waves in cavitating flows has been noted by various computational and experimental studies (Jakobsen, 1964; Kawanami et al., 1997; Reisman et al., 1998; Arndt et al., 2000). Recently, the experiments of Ganesh et al. (2016) showed bubbly shock propagation as a mechanism for sheet to cloud transition, in addition to the classically observed re-entrant jet. This motivated various computational studies on the same configuration (Gnanaskandan and Mahesh, 2016b; Schenke and van Terwisga, 2017; Budich et al., 2018). Gnanaskandan and Mahesh (2016b) simulated the experimental configuration of Ganesh et al. (2016) in the transitory regime, using the compressible LES approach. They provided detailed description of the re-entrant jet induced transition including flow reversal due to adverse pressure gradient, intermittent nature of the pressure waves and baroclinic vorticity production. However, they do not discuss bubbly shock wave phenomenon. Budich et al. (2018) studied the experimental configuration in the periodic regime using the compressible Euler equation with a barotropic equation of state, capturing the bubbly shock waves in their simulations. In accordance with the experiments, they showed that bubbly shocks are locally supersonic and satisfy the Rankine–Hugoniot jump conditions. However, they do not use subgrid scale model and do not discuss re-entrant jet phenomenon. Schenke and van Terwisga (2017) presented a model to capture compressible effects using an incompressible solver with finite rate mass transfer. They also performed simulations in the periodic regime and provided useful discussion of finite rate mass transfer effects on shedding frequency and vapor content. Experimentally, bubbly shock wave propagation was also observed by Jahangir et al. (2018) in partial cavitation inside a nozzle and Wu et al. (2017) in a 2D converging-diverging section. Interestingly, Jahangir et al. (2018) and Wu et al. (2017) observe initiation of bubbly shock wave by the impingement of collapse-induced pressure waves from previously shed clouds.

A number of computational studies have used RANS (Reynolds Averaged Navier–Stokes) models along with the homogeneous mixture assumption for the study of sheet to cloud cavitation (e.g. Singhal et al., 2002; Saito et al., 2007; Schnerr et al., 2008; Seo and Lele, 2009; Goncalves and Patella, 2009; Kim, 2009). However, standard RANS models require modifications to eddy viscosity for predicting cloud cavitation (Coutier-Delgosha et al., 2003). Gnanaskandan and Mahesh (2016b) compare RANS and LES in the Ganesh et al. (2016) configuration, and demonstrate that LES shows better results for volume fraction compared to RANS. In recent years, LES has shown promising results for capturing the wide range of scales and unsteady nature of cavitating flows (e.g. Bensow and Bark, 2010; Gnanaskandan and Mahesh, 2016b; Wang et al., 2016; Pendar and Roohi, 2018; Long et al., 2019). In addition, comparative studies conducted using different turbulence models have also suggested the suitability of LES over other approaches (e.g Eskilsson and Bensow, 2012; Gnanaskandan and Mahesh, 2016a; Asnaghi et al., 2017).

The goals of the present study are to: (i) Evaluate the finite rate homogeneous mixture model using compressible LES (Gnanaskandan and Mahesh, 2015) over the diverse range of incipient, transitory and periodic cavitation regimes observed in the experimental configuration of Ganesh et al. (2016). This includes capturing both the re-entrant jet and the bubbly shock waves as instability mechanisms of cloud cavitation. Also, perform quantitative comparison to the experimental data for the vapor volume fraction, shedding characteristics and bubbly shock propagation speeds. (ii) Use the LES flow field to investigate the conditions that lead to either the formation of re-entrant jet or bubbly shock wave. (iii) Study the initiation of bubbly shock wave by the collapse-induced pressure wave from previously shed clouds.

The paper is organized as follows. Section 2 describes the governing equations, physical model and numerical method used in

the simulations. Section 3 describes the computational domain, grid and the inflow/outflow comparisons. Section 4 discusses the instantaneous solution obtained from LES, comparison to experiments, results comparing different flow regimes and mechanisms governing sheet to cloud transition. The paper is summarized in Section 5.

2. Governing equations and physical model

We use the homogeneous mixture approach where the mixture of water and vapor is considered as a single compressible medium. We assume mechanical equilibrium (i.e. each phase has the same pressure as the cell pressure and slip velocity between the phases is not considered) and thermal equilibrium (i.e. temperature of each phase is same as the cell temperature). Note that the Weber number ($We = \rho u^2 l/S$) of the simulations conducted in the current study is very high ($O(10^4)$) based on liquid density ($\rho = 1000$ kg/m^3), surface tension ($S = 0.07$ N/m^2), length scale ($l = 0.0254$ m) and velocity scale ($u = 8$ m/s). Hence, surface tension effects are generally very small. Assuming a homogeneous mixture, subgrid scale bubble dynamics and surface tension effects are thus neglected. In hydrodynamic cavitation, due to the high specific heat capacity of the water, medium causes only minor temperature fluctuations. Hence, an isothermal formulation is used to reduce simulation time.

The governing equations are the compressible Navier–Stokes equations for mixture quantities along with the transport equation for vapor mass fraction:

$$\begin{aligned}
\frac{\partial \rho}{\partial t} &= -\frac{\partial}{\partial x_j}(\rho u_j),\\
\frac{\partial \rho u_i}{\partial t} &= -\frac{\partial}{\partial x_j}(\rho u_i u_j + p\delta_{ij} - \sigma_{ij}),\\
\frac{\partial \rho Y_v}{\partial t} &= -\frac{\partial}{\partial x_j}(\rho Y_v u_j) + S_e - S_c.
\end{aligned} \tag{1}$$

Here ρ, u_i and p are density, velocity, and pressure of the mixture respectively, and Y_v is the vapor mass fraction. The mixture density is defined as

$$\rho = \rho_l(1-\alpha_v) + \rho_v\alpha_v, \tag{2}$$

where ρ_l and ρ_v are densities of liquid and vapor respectively, and α_v is the volume fraction of vapor. Volume fractions of each constituent phase are related to their respective mass fractions by

$$\rho_l(1-\alpha_v) = \rho(1-Y_v) \quad \text{and} \quad \rho_v\alpha_v = \rho Y_v. \tag{3}$$

The system is closed using a mixture equation of state obtained using a stiffened equation of state for the liquid, and ideal gas equation of state for vapor:

$$p = Y_v\rho R_v T + (1-Y_v)\rho K_l T\frac{p}{p+P_c}, \tag{4}$$

where $K_l = 2684.075$ J/(Kg K) and $P_c = 786.333 \times 10^6$ Pa are the constants associated with equation of state for the liquid. The parameters were derived by Gnanaskandan and Mahesh (2015) to match speed of sound in liquid at prescribed density to NIST data. Gnanaskandan and Mahesh (2015) also validated the thermodynamic model for a variety of problems including sheet to cloud cavitation. $R_v = 461.6$ J/(KgK) is the specific gas constant for equation of state of vapor obtained from Saito et al. (2007). The viscous stress tensor (σ_{ij}) is given by

$$\sigma_{ij} = \mu\left(\frac{\partial u_i}{\partial x_j} + \frac{\partial u_j}{\partial u_i} - \frac{2}{3}\frac{\partial u_k}{\partial x_k}\delta_{ij}\right), \tag{5}$$

where the mixture viscosity is defined as

$$\mu \quad = \mu_l(1-\alpha_v)(1+2.5\alpha_v) + \mu_v\alpha_v, \quad \text{and} \tag{6}$$

μ_l and μ_v are the dynamic viscosity of water and vapor respectively. S_e and S_c are source terms for evaporation of water and condensation of vapor and are given by

$$\begin{aligned}
S_e &= C_e\alpha_v^2(1-\alpha_v)^2\frac{\rho_l}{\rho_g}\frac{\max((p_v-p),0)}{\sqrt{2\pi R_g T}},\\
S_c &= C_c\alpha_v^2(1-\alpha_v)^2\frac{\max((p-p_v),0)}{\sqrt{2\pi R_g T}},
\end{aligned} \tag{7}$$

where $p_v = 2.3$ kPa is the vapor pressure. $C_e(1/m)$ and $C_c(1/m)$ are empirical constants based on the interfacial area as defined by Saito et al. (2007). We non-dimensionalize the empirical constants based on the characteristic length scale of the problem as $1/h = 36.5$ 1/m, where $h = 1$ inch is the wedge height. The mixture speed of sound is obtained using mixture equation of state (Eq. (4)) and Gibbs equation. The sound speed is obtained assuming no mass transfer between the phases and hence is the frozen speed of sound. Due to finite rate of phase change, speed of sound in a water-vapor mixture is lower than the limiting value of frozen sound speed (Franc and Michel, 2005). Sound speed in such case depends on accurate rate of phase change, subgrid scale bubble dynamics and non-condensable gas nuclei. Hence, it is often problem dependent. The accurate measurement of the speed of sound experimentally, in a highly unsteady flows such as considered in the current work is quite involved. In addition, analytical expressions for the speed of sound provide values in the limit of no mass transfer (i.e. frozen speed of sound) and equilibrium mass transfer (i.e. equilibrium speed of sound) (Franc and Michel, 2005).

The numerical method is a predictor corrector approach developed by Gnanaskandan and Mahesh (2015) to simulate cavitating flows on unstructured grids. The predictor step uses a non-dissipative finite volume scheme and the corrector step uses characteristic based filtering as a shock capturing scheme to control dissipation locally in the vicinity of contact discontinuities and shocks. Governing equations (Eq. (1)) are spatially Favre-filtered for LES and subgrid terms are modeled using the Dynamic Smagorinsky model (DSM) (Moin et al., 1991). Details of the numerical method and validation for a variety of flow problems are provided by Gnanaskandan and Mahesh (2015).

3. Problem setup

3.1. Computational setup and simulation details

Fig. 2 shows a schematic of the computational setup. The apex of the wedge is located at (0, h, 0), where h (1 inch) is the wedge height. The mean flow direction is along the positive x-axis. Flow enters the domain through a $3h \times 3h$ cross section ($y-z$ plane) which corresponds to the reduced test section in the experiments of Ganesh et al. (2016). The experimental test section is highlighted by $y-z$ planes (in red) towards the inflow and outflow in Fig. 2(a), a magnified view of which is shown in Fig. 2(b). The computational domain is extended upstream for 52.5 h and downstream for 57 h from the wedge apex in order to minimize the reflection of acoustic waves from the boundaries. In addition, acoustically absorbing sponge layers of length 20 h are applied at both inlet and outlet boundaries as indicated by $y-z$ planes (in green) in Fig. 2(a). This adds an additional term $\Gamma(q-q_{ref})$ in the governing equations (Eq. (1)). Here 'q' denotes the vector of conservative variables and the subscript '*ref*' denotes the reference solution. In current simulations, the reference solution corresponds to the inlet and the outlet boundary conditions. 'Γ' denotes the amplitude of the forcing. The inflow plane in the experiments is located 3.5 h upstream of the wedge apex and the outflow plane is located 22 h downstream of the wedge apex as shown in Fig. 2(b). Velocity profile measurements are performed 3.25 h upstream of the

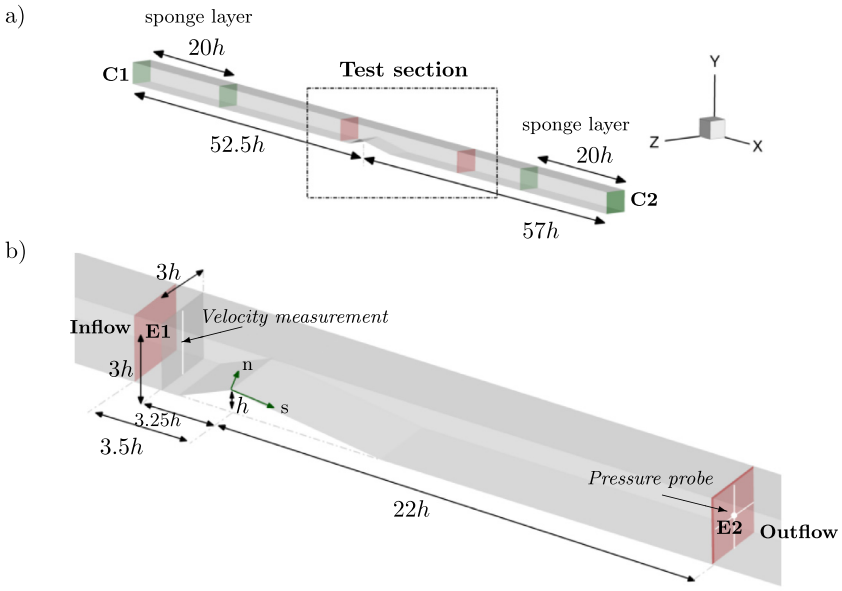

Fig. 2. Schematic of the computational domain to scale. a) Complete domain and b) magnified view of the test section.

wedge apex. '*s*' and '*n*' denote directions parallel and perpendicular to the wedge surface respectively. The wedge has contraction angle of 22.1° and diffuser angle of 8.1°. Computational planes at inlet and outlet are indicated by C1 and C2 respectively, and experimental planes for inflow and outflow comparison are indicated by E1 and E2 respectively.

The computational mesh consists of approximately 3 million hexahederal cells. The mesh is refined in the convergent-divergent section of the wedge with minimum spacing of 0.005 h (~0.125 mm) in both streamwise and wall-normal directions, near the wedge apex. A wall-normal spacing of 0.005 h is chosen to sufficiently capture the re-entrant jet. The wall normal spacing stretches to 0.03 h (~0.75 mm) at a distance 0.5h (~13 mm) normal to the wedge surface to maintain finer resolution within the vapor sheet cavity. Beyond 0.5*h*, nearly uniform spacing of 0.05h (~1.3 mm) is maintained in all the directions within the divergent section of the wedge. The grid is coarsened beyond the experimental inflow/outflow planes to assist in dampening of acoustic reflections from computational boundaries.

The flow is simulated at Reynolds number $Re = \frac{\rho_\infty u_\infty h}{\mu_\infty} = 203000$, where the subscript '$\infty$' represents free stream values. Incipient, transitory and periodic cloud shedding is considered with changes in σ_b. Details of the time step, total run time, number of shedding cycles for each regime are presented in Table 1. Note that this only includes the simulation time after initial transients have subsided and cloud shedding is established.

3.2. Inflow/outflow comparison

Computational inlet C1 is located upstream of the experimental inflow E1 and similarly, computational outlet C2 is located downstream of the experimental outflow E2. Hence, boundary conditions cannot be directly prescribed based on experimental values at E1 and E2, instead, computational inlet/outlet (C1 and C2) conditions are iteratively changed in order to match the inflow/outflow conditions at planes E1 and E2 with the experiments. In order to accelerate the process of iteratively prescribing inflow-outflow, the solution is first obtained in a two dimensional configuration, and interpolated along the span to provide initial conditions to the LES. Details of the results obtained in 2D and comparison to the experimental data is given in Bhatt and Mahesh (2018). One could also consider two dimensional RANS results for initializing LES (e.g. Gnanaskandan and Mahesh, 2016b). The pressure drop across the wedge is different in 2D as compared to the 3D; it has different blockage effects from the sheet/cloud transition and order of magnitude differences in the collapse pressures (e.g. Bhatt et al., 2015). Hence, the interpolated solution needs to adjust further to the computational inlet/outlet boundary conditions. This process however, is quicker than iterating the inlet/outlet directly in the 3D simulations. Results are analyzed after the periodic cloud shedding is established at given inflow/outflow conditions.

Spatially uniform inflow velocity is prescribed at computational inlet C1, and changed iteratively to match the mean inflow velocity at the geometric center of the inflow plane E1 as provided in the experiments. The velocity is averaged for approximately 10 cavity shedding cycles for each regime and compared to experiments in Table 2. In addition, we compare the velocity profile along the wall normal direction with Laser Doppler Velocimetry (LDV) data from Ganesh et al. (2016) at the mid-line of the $x = -3.25$ h plane indicated in Fig. 2(b). The comparison is shown in Fig. 3. Note that the deceleration of the flow near the bottom wall of wedge is captured in the numerical results. Also, the profiles are not affected by the cloud shedding regimes and compare well within the experimental uncertainties. Due to the subsonic nature of the inflow

Table 1
Details of simulations conducted.

Regime	σ_b	Time step (tu_∞/h)	Time units	Shedding cycles (approximate)	Total run-time CPU hours (10^5)
Incipient	2.47	1.0×10^{-5}	40 (0.125 s)	–	0.82
Transitory	1.89	2.5×10^{-5}	100 (0.3 s)	9–10	1.32
Periodic I	1.78	2.5×10^{-5}	160 (0.5 s)	10	2.2
Periodic II	1.59	2.5×10^{-5}	160 (0.5 s)	8–9	2.2

Table 2
Inflow/outflow comparison with the experiments. σ_b is obtained from the back pressure values (from direct communication with H. Ganesh).

	Inflow (E1): u_I (m/s)		Outflow (E2): σ_b	
	Exp.	LES	Exp.	LES
Incipient regime	8.0 ± 0.06	8.1	2.38 ± 0.06	2.47
Transitory regime	7.9 ± 0.09	8.05	1.82 ± 0.06	1.89
Periodic regime I	7.9 ± 0.18	8.01	1.73 ± 0.11	1.78
Periodic regime II	7.9 ± 0.16	8.06	1.60 ± 0.10	1.59

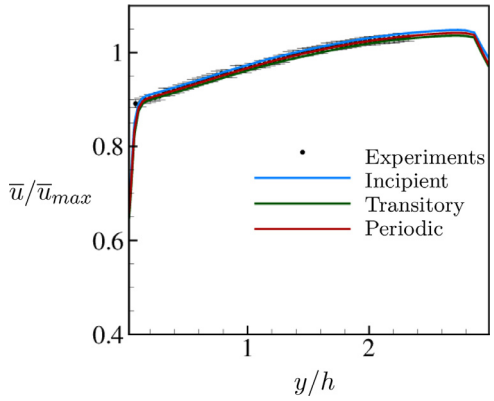

Fig. 3. Comparison of the inflow velocity profile at velocity measurement plane ($x = -3.25h$ as indicated in Fig. 2(b)) with the LDV measurements of experiments (Ganesh et al., 2016).

one of the characteristics is directed towards the inlet from within the domain. Hence, pressure cannot be directly prescribed at inlet boundary. In the simulations, we adjust the back pressure at computational outlet plane E2 in order to match the back cavitation number at outflow plane E1. Back cavitation number σ_b is defined as $\sigma_b = \frac{p - p_v(T)}{1/2\rho_\infty u_I^2}$. Here, u_I is the inflow velocity. σ_b is reduced to progress from incipient cavitation towards periodic cloud shedding as shown in Table 2. With reduction in σ_b, the experimental uncertainty in u_I and σ_b increases. Numerical values show good comparison to the inflow/outflow conditions in the experiments. The remaining domain boundaries (top/bottom and span) are treated as walls with no-slip velocity boundary conditions.

4. Results

4.1. Partial cavitation regimes

We present LES results for incipient, transitory and periodic regimes. The section illustrates how LES captures the physical characteristics of each regime observed in the experiments (Ganesh et al., 2016). We show that in the incipient regime, LES captures the cavitation inside the spanwise vortices. In the developed cavitation regimes, LES captures both the instability mechanisms (re-entrant jet and bubbly shock wave) of sheet to cloud transition as observed in the experiments.

4.1.1. Incipient cavitation

First, we consider $\sigma_b = 2.47$. An instantaneous solution of the incipient cavitation is shown in Fig. 4. The cavity is indicated by isocontours of α_v and pressure is plotted on the side plane. Note that no attached sheet cavity is observed at this σ_b, instead cavitation is observed intermittently downstream of the wedge apex particularly within the shear layer, as the local pressure drops below vapor pressure. Spanwise cavitating structures are observed within the low pressure cores of rolled up vortices inside the shear layer (as observed in Ganesh et al., 2016). It is important to distinguish

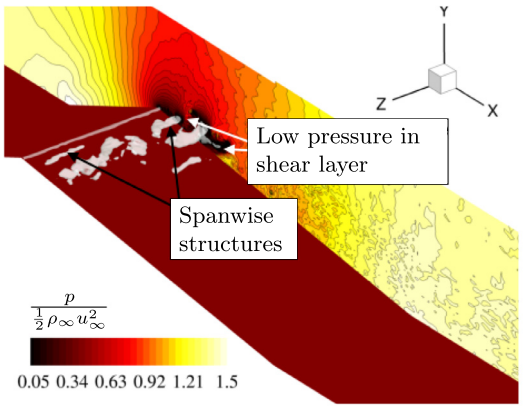

Fig. 4. Incipient cavitation. Iso-contour level $\alpha_v = 0.1$ with pressure plotted on side plane ($x - y$ plane at $z = 2.9h$).

this regime from cavitation inception in that it is a low volume fraction bubbly mixture.

4.1.2. Transitory regime

As σ_b is dropped to 1.89, a vapor sheet cavity forms that is attached to the wedge apex (Fig. 5(a)). There is noticeable variation along the span as evident from the isocontours of α_v. Vapor volume fraction data is spanwise averaged ($\langle\alpha_v\rangle$) in order to provide similar visualization as the X-ray measurements. Here, '$\langle\rangle$' denotes spanwise averaged quantities. High levels of vapor production are observed in the shear layer, while the rest of the cavity displays smaller vapor production and relatively smaller values of $\langle\alpha_v\rangle$ (~0.45). A re-entrant jet forms aft of the cavity as the liquid flow re-attaches as indicated in Fig. 5(b). Also, note the cavity perturbation due to the interaction with intermittent pressure waves. Gnanaskandan and Mahesh (2016b) discuss the intermittent nature of the pressure waves in detail, for the transitory shedding. The re-entrant jet moves upstream towards the mid-cavity leading to the transition of the aft portion of the sheet cavity into the cloud (Fig. 5(c)). $\langle\alpha_v\rangle$ within the cavity remains in the range ~0.4–0.6 and vapor production is observed intermittently inside the cavity and shear layer. Spanwise roll-up of the detached cloud and, the subsequent formation of a new vapor sheet cavity are visualized in Fig. 5(d) and (e)). The overall shedding cycle is approximately 20 ms in duration.

4.1.3. Periodic shedding

With further reduction in σ_b, the sheet to cloud transition exhibits periodic behavior. We consider periodic shedding at $\sigma_b = 1.78$. Fig. 6(a) shows the beginning of cavity growth from the wedge apex. The detached cloud from the previous cavity rolls up and advects downstream accompanied by growth of the vapor cavity (Fig. 6(b)). Fig. 6(c) shows an instant when the cavity reaches its maximum length. It is interesting to note that the grown cavity is nearly two-dimensional with stable cavity interface, while three dimensionality is observed in the cavity closure region and in the detached cloud. In addition, high values of $\langle\alpha_v\rangle$ (~0.8-0.9) are observed inside the entire cavity (also observed in the experiments of Ganesh et al., 2016) along with significant vapor production indicated by $\langle Y_v\rangle$. Complete collapse of the vapor cloud (visible in Fig. 6(c)) is shown in 6(d). High pressure regions due to the cloud collapse are noticeable on the side plane. Collapse-induced pressure waves impinge on the trailing edge of the cavity, initiating the cavity retraction by a condensation front. Spanwise variation in the condensation front as it propagates towards the wedge-apex can be observed in Fig. 6(e). Note that transitory shedding also exhibits condensation front induced sheet to cloud transition

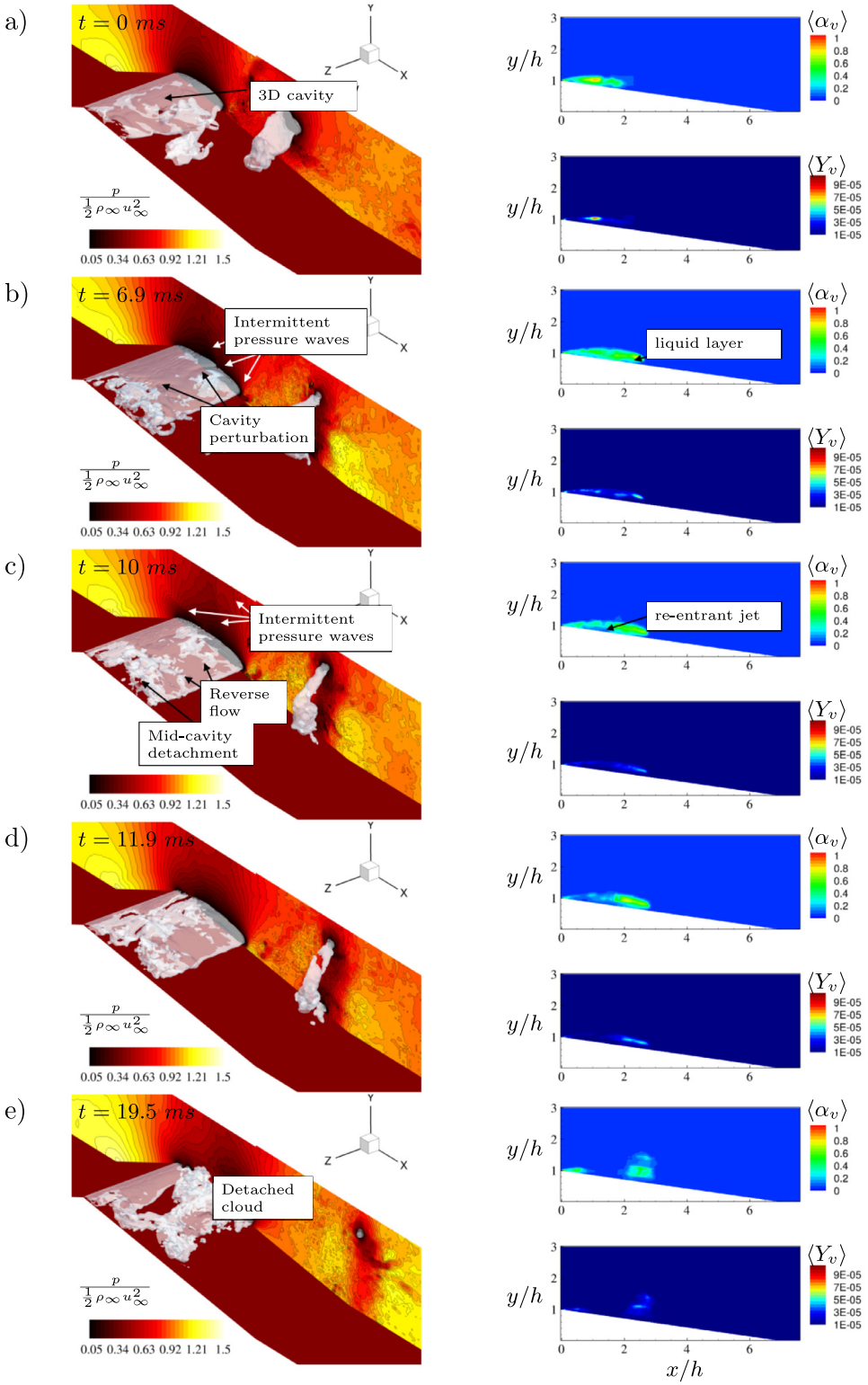

Fig. 5. Transitory shedding cycle. (On left) Iso-contour level $\alpha_v = 0.1$ with pressure plotted on side plane ($x - y$ plane at $z = 2.9$ h) and (on right) spanwise averaged vapor volume fraction ($\langle\alpha_v\rangle$) and vapor mass fraction ($\langle Y_v\rangle$). a) Sheet cavity growth ($t = 0$ ms), b) maximum cavity length ($t = 8$ ms), c) re-entrant jet induced sheet to cloud transition ($t = 10$ ms), d) detached cloud ($t = 11.9$ ms) and e) new cycle of sheet growth ($t = 19.5$ ms).

along with the re-entrant jet induced shedding. However, periodic shedding is observed predominantly due to the condensation front propagation. The behavior is apparent at lower σ_b (e.g. $\sigma_b = 1.59$). In the current section, only representative shedding cycles are considered.

4.2. Comparison to the experiments

We compare the mean volume fraction data to the X-ray measurements of Ganesh et al. (2016). In addition, we consider the time evolution of instantaneous vapor volume fraction, condensa-

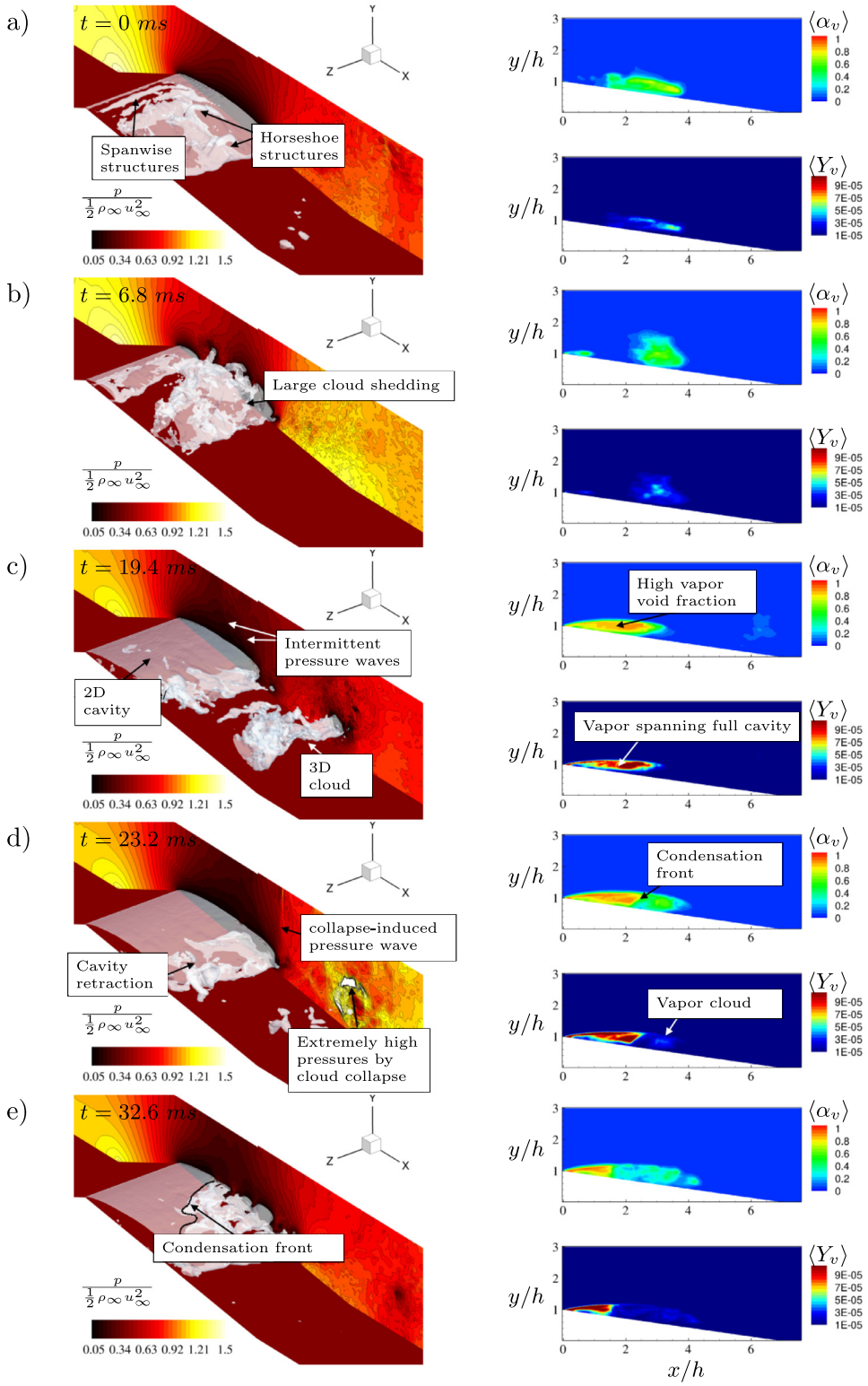

Fig. 6. Periodic shedding cycle. (On left) Iso-contours level $\alpha_v = 0.1$ with pressure plotted on side plane ($x-y$ plane at $z = 2.9$h) and (on right) spanwise averaged vapor volume fraction ($\langle\alpha_v\rangle$) and vapor mass fraction ($\langle Y_v\rangle$). a) Detached cloud (previous cycle) ($t = 0$ ms), b) cavity growth ($t = 6.8$ ms), c) Complete cavity growth ($t = 19.4$ ms), d) Initiation of cavity retraction ($t = 23.2$ ms) and e) sheet to cloud transition due to the propagation of condensation front ($t = 32.6$ ms).

tion front speed and the frequency of periodic shedding for comparison to the experimental data.

4.2.1. Comparison to X-ray densitometry

The mean vapor volume fraction is compared to experiments in Figs. 7–9 for incipient, transitory and periodic regimes respectively. For each case, contours of time average of spanwise averaged vapor volume fractions ($\overline{\langle\alpha_v\rangle}$) obtained from LES are plotted alongside the time averaged X-ray measurement data. Here '$\bar{\ }$' denotes time average. The field of view of the X-ray measurement is matched to LES and contour levels are identical. In addition, profiles of $\overline{\langle\alpha_v\rangle}$ extracted along the y axis from the wedge surface at various ax-

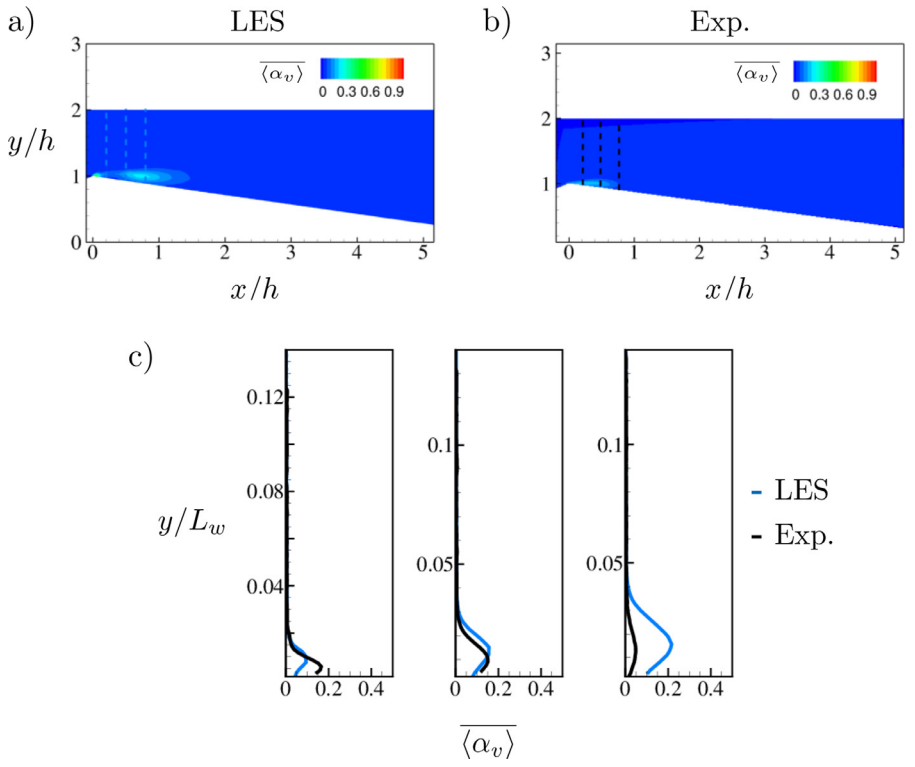

Fig. 7. Incipient regime : comparison of time average of spanwise averaged vapor volume fraction $\overline{\langle\alpha_v\rangle}$. a) Contours of $\overline{\langle\alpha_v\rangle}$ from LES at $\sigma_b = 2.47$, b) time average of X-ray measurements at $\sigma_b = 2.38 \pm 0.06$ as indicated in Table 2 (data obtained from direct communication with H.Ganesh) and c) comparison of profiles extracted at $s/L_w = 0.03, 0.06$ and 0.09, indicated by the dashed lines in the contour plots.

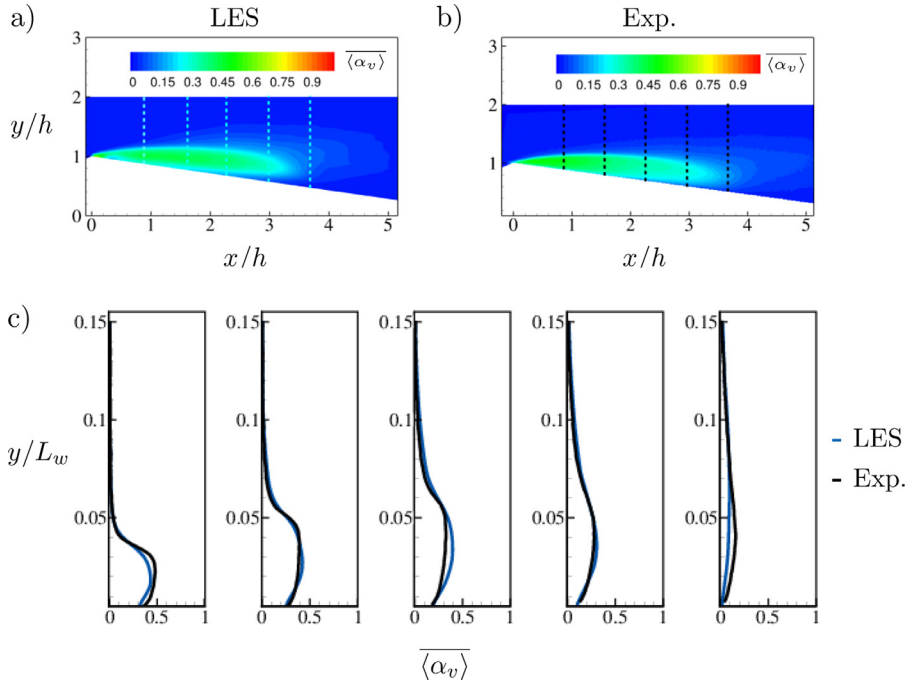

Fig. 8. Transitory shedding : comparison of time average of spanwise averaged vapor volume fraction $\overline{\langle\alpha_v\rangle}$. a) Contours of $\overline{\langle\alpha_v\rangle}$ from LES at $\sigma_b = 1.89$, b) time average of X-ray measurements at $\sigma_b = 1.82 \pm 0.06$ as indicated in Table 2 (data obtained from direct communication with H.Ganesh) and c) comparison of the profiles extracted at $s/L_w = 0.1, 0.2, 0.3, 0.4$ and 0.5, indicated by the dashed lines in the contour plots.

ial locations are plotted in Figs. 7(c), 8(c) and 9(c). For each case, LES statistics are sampled at $0.005tu_\infty/h$ (~0.015 ms), which provides sufficient temporal resolution to capture variations in cavity size over a given cycle for comparison to the X-ray measurements sampled at 1 ms. Statistics are averaged over approximately 10 shedding cycles (which corresponds to the physical time of $0.5s$ for the periodic shedding case) to capture the low frequency of cloud shedding. Table 1 shows details of the total run for each regime. Experimental results are taken for total time of 0.79 s, which corresponds to approximately 16 shedding cycle for periodic shedding.

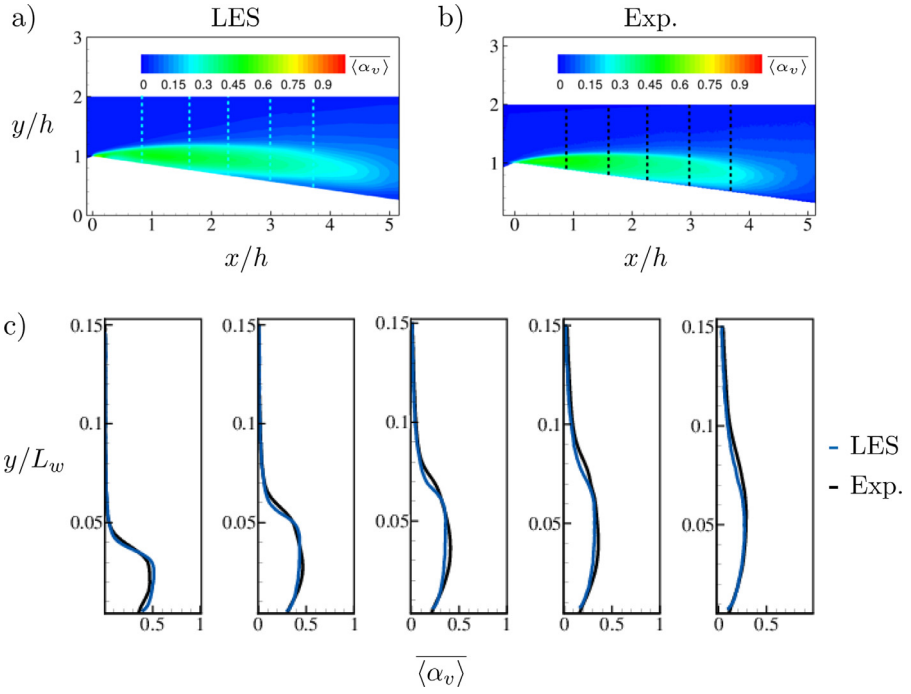

Fig. 9. Periodic shedding : comparison of time average of spanwise averaged vapor volume fraction $\overline{\langle\alpha_v\rangle}$. a) Contours of $\overline{\langle\alpha_v\rangle}$ from LES at $\sigma_b = 1.78$, b) time average of X-ray measurements at $\sigma_b = 1.73 \pm 0.11$ as indicated in Table 2 (data obtained from direct communication with H.Ganesh) and c) comparison of the profiles extracted at $s/L_w = 0.1, 0.2, 0.3, 0.4$ and 0.5, indicated by the dashed lines in the contour plots.

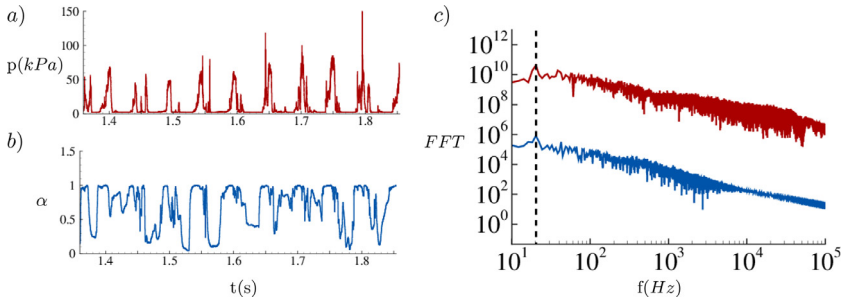

Fig. 10. Frequency of shedding. a) p(t), b) $\alpha(t)$ taken at (3h, 1.5h, 1.5h) and c) corresponding FFT (p -, α -).

Table 3
Comparison of cavity length and thickness based on isocontour level of $\overline{\langle\alpha_v\rangle} = 0.25$ for transitory and periodic regime.

Regime	Cavity length (mm)		Cavity thickness (mm)	
	LES	Exp	LES	Exp
Transitory	76.86	75.96	10.18	10.05
Periodic I	102.35	93.38	12.30	11.76

Fig. 7 shows the comparison for the incipient regime. Volume fraction levels within the cavity are very small (less than ~0.2) both in the simulations and the experiments. The larger cavity in the simulation compared to the experiments can possibly be due to increased sensitivity of the incipient regime to inflow/outflow conditions and free stream nuclei content. Figs. 8 and 9 respectively, show comparison for the transitory and the periodic regimes. In both regimes, as discussed in the Section 4.1, overall larger regions of vapor are formed (e.g. a sheet cavity of vapor over a wedge surface and cloud shedding downstream). Mean volume fractions within the cavity range from ~0.3 to ~0.6, with higher values particularly within the sheet region. Cavity length/thickness is obtained by considering an isocontour level of $\overline{\langle\alpha_v\rangle} = 0.25$ both in the experiments and in the simulations and is shown in 3. Considering cycle to cycle variation in sheet/cloud cavitation in each regime (also observed in Ganesh et al. (2016)) and the unsteady nature of the flow, the comparison in the cavity length and thickness is encouraging. In addition, distribution of vapor volume fraction in the divergent section of the wedge show very good comparison in the free stream, within the cavity and also near the surface of the wedge. This is indicated by $\overline{\langle\alpha_v\rangle}$ profiles in Figs. 8(c) and 9(c).

4.2.2. Characteristics of shedding and condensation front

The frequency of periodic shedding of the cloud at $\sigma_b = 1.784$ is computed from Fast Fourier Transform (FFT) of the time-varying void fraction and pressure signal at (3h, 1.5h, 1.5h) inside the cavity. The signals for the pressure and the void fraction are shown in Fig. 10(a) and (b) respectively. The corresponding FFT is shown in Fig. 10(c). The signal shows periodic pressure pulses followed by low pressure (vapor pressure ~2 kPa) regions spanning approximately 10 cycles taken over 0.5 s. FFT of both the signals (α and p) show peaks at identical values of $f = 20.13$ Hz, indicating that the cavity shedding mechanism is associated with the propagation of pressure pulses. The Strouhal number for the cavity shedding is obtained as $St = fL_{cav}/u_I$. Here, L_{cav} is obtained based on isocontour level $\overline{\langle\alpha_v\rangle} = 0.25$ as defined in Section 4.2.1. u_I is shown in Table 2. We compute St for the experiment in an identical manner to maintain the same definition of L_{cav} and u_I. Table 4 shows that

Table 4
Comparison of characteristics of shedding and condensation front with experiments.

Shedding characteristics				Condensation front			
Frequency		Strouhal number ($St_{L_{cav}}$)		Shock speed		Sound speed	Mach
Exp.	LES	Exp.	LES	Exp.	LES		
20.00 *Hz*	20.13 *Hz*	0.240	0.256	4.5 *m/s*	5.0 *m/s*	3.34 *m/s*	1.49

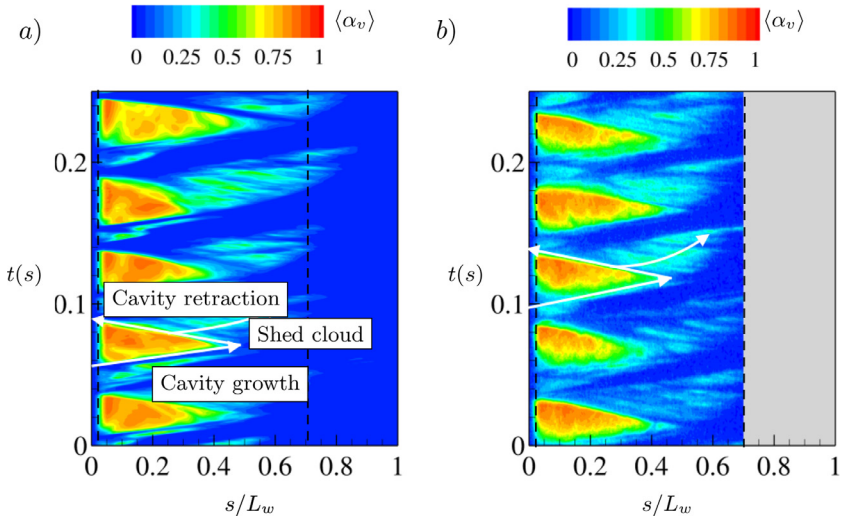

Fig. 11. Temporal evolution of $\langle\alpha_v\rangle$ taken on a line parallel to the wedge surface at a normal distance $n = 4$ mm for 0.25 s showing approximately 5 cavity shedding cycles. a) LES, b) X-ray measurements (from direction communication from H.Ganesh). Black dashed line is used to indicate the wedge apex and edge of X-ray measurement frame.

shedding characteristics obtained from the LES compare well with the experiments.

The time evolution of cavity shedding over multiple cycles can be analyzed by considering temporal evolution of the spanwise-averaged flow field. We consider a line parallel to the wedge surface at a normal distance $n = 4$ mm and stack the solution for multiple time instances, constructing an $s - t$ diagram. Fig. 11 shows time evolution of $\langle\alpha_v\rangle$ for LES and X-ray measurement plotted side by side. The triangular region of $\langle\alpha_v\rangle$ indicates 1 cycle of cavity shedding. The cavity growth and collapse within the cycle is indicated by white arrows. Variations in cavity length and vapor volume fraction distribution are observed from cycle to cycle in both the simulation and in the experiment. It is observed that $\langle\alpha_v\rangle$ inside the cavity reaches values greater than 0.75, while regions within the cloud have $\langle\alpha_v\rangle$ in the range $0.25 - 0.5$. In addition, the slopes of isocontour lines during cavity growth and retraction can be used to compute the respective speeds. The inverse of the slope in the $s - t$ diagram (Fig. 11) for cavity retraction indicates condensation front speed in the laboratory frame of reference. This is, assuming that the flow speed inside the cavity is negligible. Condensation front speed thus obtained is averaged over 10 shedding cycles for both the experiment and the simulation and good comparison is obtained as shown in Table 4. The sound speed of high volume fraction liquid-gas mixture is orders of magnitude smaller than its constituent phases. Mach number computed based on the frozen speed of sound is greater than 1. This indicates that the condensation front is supersonic and hence a shock wave. This volume fraction discontinuity traveling at a supersonic speed is referred as a "bubbly shock wave".

4.3. Conditions favoring the formation of re-entrant jet or bubbly shock waves

We consider the effect of reducing σ_b on the mean flow-field in the developed cavitation regimes (transitory, periodic I and periodic II). We discuss conditions favoring the formation of either the re-entrant jet or bubbly shock waves through streamline curvature effects, adverse pressure gradient, medium compressibility and vapor production. Results presented in Section 4.3.1–4.3.3 are time averaged data taken at $z/h = 1.5$ (i.e. in the symmetry plane).

4.3.1. Streamline curvature

Mean pressure contours inside the convergent-divergent section of the wedge are plotted in Fig. 12. Streamlines in the figure are based on the mean flow velocities for each regime. Visibly, with the reduction in σ_b, the mean cavity length increases and the mean pressure in the divergent section of the wedge decreases. Note that the lowest pressures in the divergent section are observed in the vicinity of the mid point of the cavity where flow confinement is maximum. Also note that the streamline curvature reduces with the reduction in σ_b. For periodic regime II (at $\sigma_b = 1.59$), streamlines closer to the cavity are nearly flat. We assess the effect of streamline curvature on the pressure recovery by computing pressure rise normal to the streamlines using the momentum equation in the streamline co-ordinate system. We simplify the analysis by considering the inviscid momentum equation for the mean flow as

$$\frac{\partial \overline{p}}{\partial n} = \frac{\overline{\rho}\overline{U}^2}{R}. \tag{8}$$

Here, R is the radius of curvature, which is approximated as $R(n) = R_{cav} exp^{-(n-n_0)}$. R_{cav} is the radius of curvature at the cavity interface and n_0 indicates co-ordinate at the edge of the cavity. The exponential profile tends to R_{cav} at the cavity interface and to nearly flat streamlines at the top wall. $\overline{U}$ is the mean velocity along the streamlines. Integrating Eq. (8) from the mid cavity to the top wall as shown in Fig. 12, yields corresponding pressure rise normal to the streamlines. Note that higher curvature (lower radius of curvature) and higher mean density results in larger pressure rise (Eq. (8)). Table 5 compares the pressure rise obtained

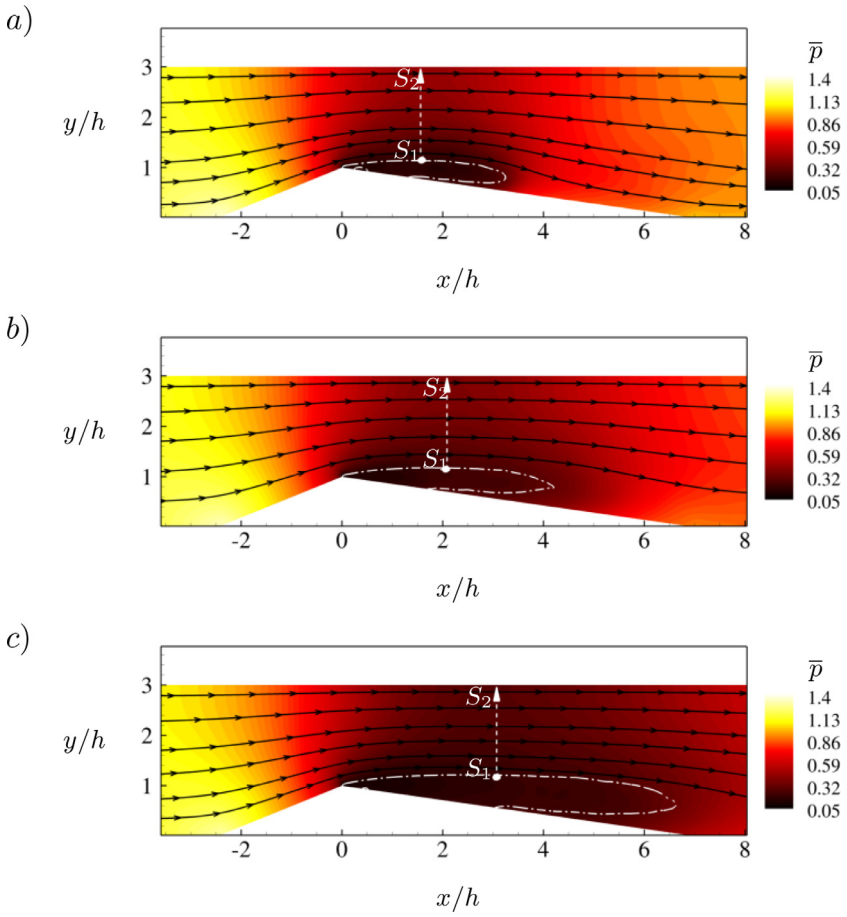

Fig. 12. Streamline curvature: contours of $\overline{p}$ for a) transitory regime, b) periodic I and c) periodic II. Dotted dashed line indicate cavity interface and dashed line indicate the direction along the measurement of pressure rise.

Table 5
Pressure estimation from streamline curvature.

	Regime	Transitory	Periodic I	Periodic II
$\overline{p}_{s_2} - \overline{p}_{s_1}$ (kPa)	Streamline curvature	17.19	10.56	4.2
	LES	18.37	11.15	5.9

from the streamline curvature estimation to the LES results. The simplified streamline curvature estimation compares reasonably to the LES results. Also, the pressure rise in the divergent section reduces significantly as one advances from the transitory to the periodic regime (Table 5). To summarize, moving from the transitory to the periodic regime, cavity growth leads to reduction in streamline curvature and consequently the reduction in pressure rise. The analysis presented here is for the mean flow. Instantaneously also, one can conceive that the pressure inside the cavity is determined by vapor pressure, and resulting curvature of the cavity influences the pressure rise beyond the cavity into the divergent section of the wedge. Profiles of pressure recovery (for the analysis presented in 4.3.1) from 'S1' to 'S2' are plotted in Fig. 13. The pressure within the cavity is order of few kPa (close to vapor pressure). Periodic shedding II shows that the pressure only recovers as much as ~ 5 kPa normal to the cavity (also shown in Table 5).

4.3.2. Pressure recovery

Here, we compare mean adverse pressure gradient (or pressure recovery) in the cavity closure region for the transitory and the periodic shedding. The analysis to obtain pressure rise based on the streamline curvature as discussed in Section 4.3.1 is non-trivial along the axial direction due to the difficulty in accurately estimating curvature and high turbulent intensities. Results obtained directly from the LES are plotted along a line parallel to the wedge surface at a normal distance $n = 4$ mm in Fig. 13. Sharp pressure recovery in the transitory regime, compared to the slower pressure rise in the periodic regimes is evident. Hence, a high adverse pressure gradient in the transitory regime favors the formation of the re-entrant jet.

4.3.3. Medium compressibility

Next, we consider the effect of pressure recovery on medium compressibility. As discussed earlier, in the periodic regime, pressure recovery is weaker from within the cavity to outside. As a result, relatively low pressure is maintained in the divergent section of the wedge following the cavity. This is shown in Fig. 14(a) by profiles of mean pressure at $y/h = 1.5$ along the convergent-divergent section of the wedge. Significantly lower pressures are observed in the region following cavity closure. Low pressure following the cavity also leads to an increased vapor volume fraction. This forms a bubbly mixture with $\overline{\alpha_v} \sim 0.01 - 0.1$, higher values in the periodic shedding cases (Fig. 14(b)). The vapor volume fraction observed beyond cavity closure can be due to the cloud shedding and the expansion of the free stream nuclei. This low pressure bubbly mixture results in increased medium compressibility. Consider the variation in the sound speed with vapor volume fraction and pressure (plotted in Fig. 15). Sound speed drops by an order of magnitude in the bubbly mixture with the drop in pressure from 100 kPa to 2 kPa. In addition, higher vapor volume fraction further

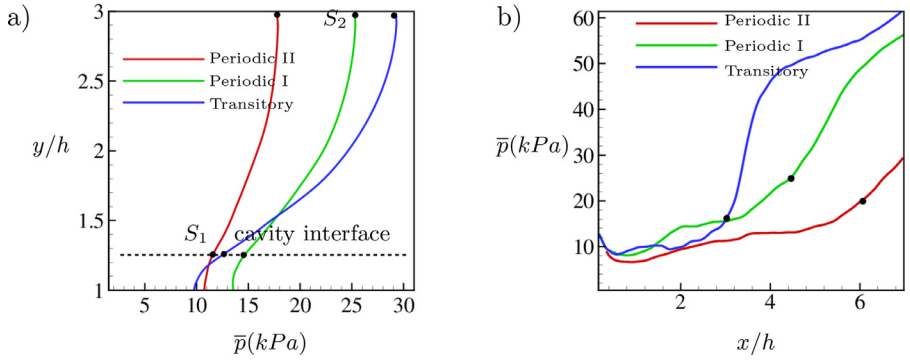

Fig. 13. Pressure rise a) normal to the cavity at mid-cavity and b) parallel to the wedge surface at a normal distance $n = 4$ mm (• indicates cavity closure). Note that cavity interface is indicated by single dotted line only for clarity, minor variations in the interface position exist for different regimes.

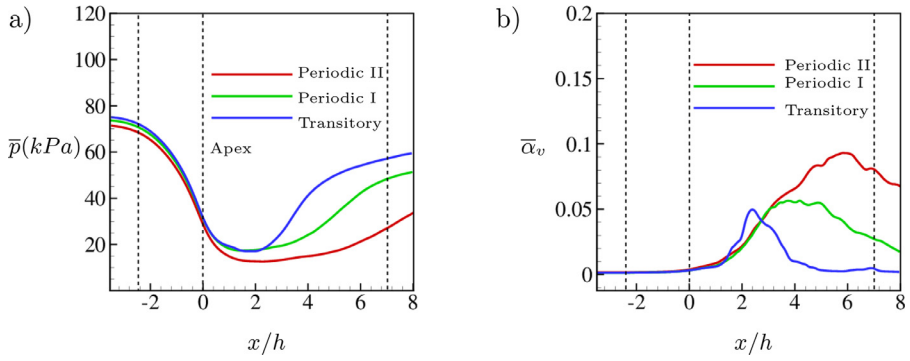

Fig. 14. Variation in the a) mean pressure and b) $\overline{\alpha_v}$ at $y/h = 1.5$ along the convergent-divergent section of the wedge.

Table 6
Sound speed variation with vapor volume fraction and pressure.

P	100 (kPa)			20 (kPa)			2 (kPa)		
α	0.01	0.05	0.1	0.01	0.05	0.1	0.01	0.05	0.1
a (m/s)	106.88	45.52	33.56	47.89	20.37	15.00	15.15	6.40	4.70

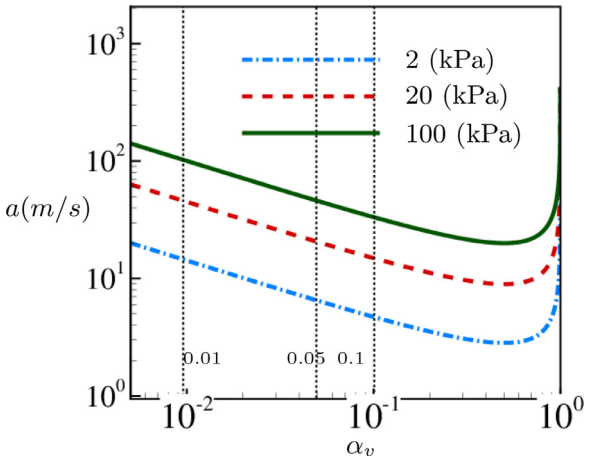

Fig. 15. Sound speed variation with vapor volume fraction and pressure.

reduces the speed of sound. As shown in Table 6, speed of sound at $p = 100$ kPa and $\alpha_v = 0.01$ is 106.88 m/s and it drops to as low as 4.7 m/s at $p = 2$ kPa and $\alpha_v = 0.1$. Consequently, as one move from the transitory to the periodic regime, the medium becomes more compressible and susceptible to the formation of shock waves.

4.3.4. Vapor production

We consider the differences in vapor production between the transitory and the periodic regimes. In the transitory regime, vapor begins to form inside the shear layer attached to the wedge apex and also intermittently within the cavity, as instantaneous pressure drops below vapor pressure (Fig. 16(a)). Vapor production averaged over an entire cycle of re-entrant jet-driven sheet to cloud shedding show high values along the shear layer and at the cavity closure inside the spanwise rolled up cloud (Fig. 16(a)). With further drop in cavitation number to $\sigma = 1.78$ in the periodic regime, vapor forms over the entire thickness of the cavity as indicated in Fig. 16(b). Vapor production averaged over an entire cycle of the bubbly shock wave is evidently different from the re-entrant jet driven shedding cycle, particularly with regard to the overall mass fraction within the cavity. Significant vapor production in the periodic regime, leads to reduction in the speed of sound favoring the formation of shocks. This is also in-line with the observation of high vapor volume fractions (~0.9) within the cavity both in the experiments (Ganesh et al., 2016) and in the LES.

We define local cavitation number as $\sigma_l = \frac{p_{loc} - p_v}{0.5\rho_\infty u_\infty^2}$, where p_{loc} is the local pressure inside a cell. At a given instant if σ_l is below 0, vapor is produced by the phase change. This also distinguishes the phase change process as compared to only expansion. We compare $\langle \sigma_l \rangle$ and $\langle Y_v \rangle$ within the cavity to identify the distinction between re-entrant jet and bubbly shock cycles. Fig. 17(a) and (b)

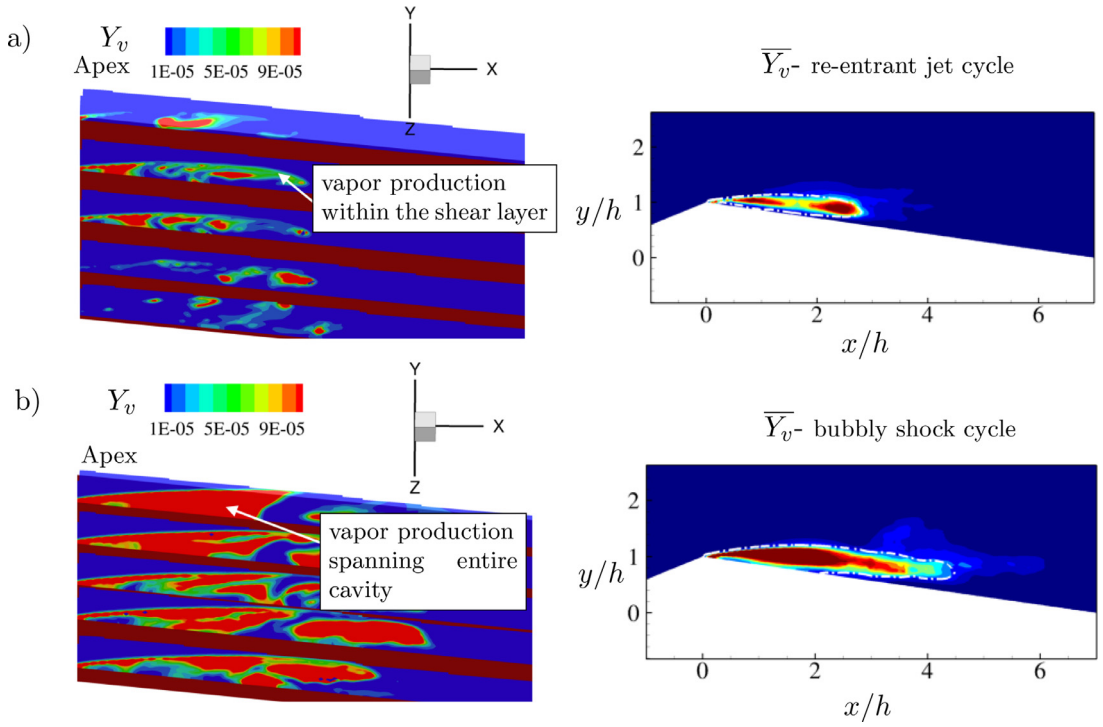

Fig. 16. Vapor production. On left are the slices along the z-axis showing instantaneous Y_v and on right are the spanwise averaged mass fraction taken over a corresponding shedding cycle in the regime. a) Transitory (re-entrant jet cycle) and b) periodic I (bubbly shock wave cycle).

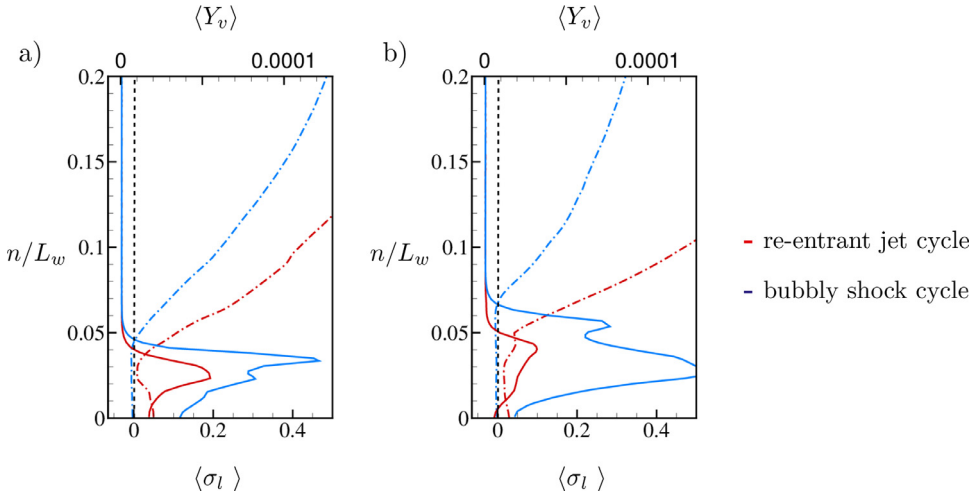

Fig. 17. Local cavitation number. a) profiles of $\langle \sigma_l \rangle$ and $\langle Y_v \rangle$ taken at $s = 0.1L_w$ normal to the wedge and b) profiles of $\langle \sigma_l \rangle$ and $\langle Y_v \rangle$ taken at $s = 0.2L_w$ normal to the wedge surface. Dotted dashed lines indicate $\langle \sigma_l \rangle$ and solid lines indicate $\langle Y_v \rangle$.

show profiles of $\langle \sigma_l \rangle$ and $\langle Y_v \rangle$ taken respectively at $s = 0.1L_w$ and $s = 0.2L_w$ normal to the wedge for both cycles. For the bubbly shock cycle, $\langle \sigma_l \rangle$ remains less than 0 (nearly constant) spanning the entire cavity, unlike the re-entrant jet cycle where σ_l tends to 0 in the shear layer at cavity interface and recovers to positive values within the rest of the cavity. In addition, vapor mass production inside the cavity is noticeably higher for the bubbly shock cycle. Nearly constant value of $\sigma_l < 0$ inside the cavity for the bubbly shock cycle can be explained by considering Eq. (8). With significant vapor inside the cavity, the overall mixture density is an order of magnitude small and consequently the resulting pressure difference from Eq. (8) is small. This is unlike the case of re-entrant jet, where in addition to the low vapor production within the cavity, density recovers by the liquid layer. In either case, regions of the shear layer (at cavity interface) show maximum vapor production. Makiharju et al. (2017) indeed observed that injection of non-condensable gas at the apex into the shear layer as compared to the injection at mid-cavity led to significant reduction in vapor production within the cavity, and consequently influencing bubbly shock propagation.

4.4. Origin of the bubbly shock waves

In the periodic regime we observed that cavity retraction is initiated by the collapse-induced pressure wave. Occurrence of this is evident at lower σ_b. We consider $\sigma_b = 1.59$ (periodic shedding II in Table 1) to explain this phenomenon. We concentrate only on the part of the cycle visualizing collapse-induced pressure waves and subsequent cavity retraction. The shedding cycle is visualized using instantaneous isocontours of vapor volume fraction along

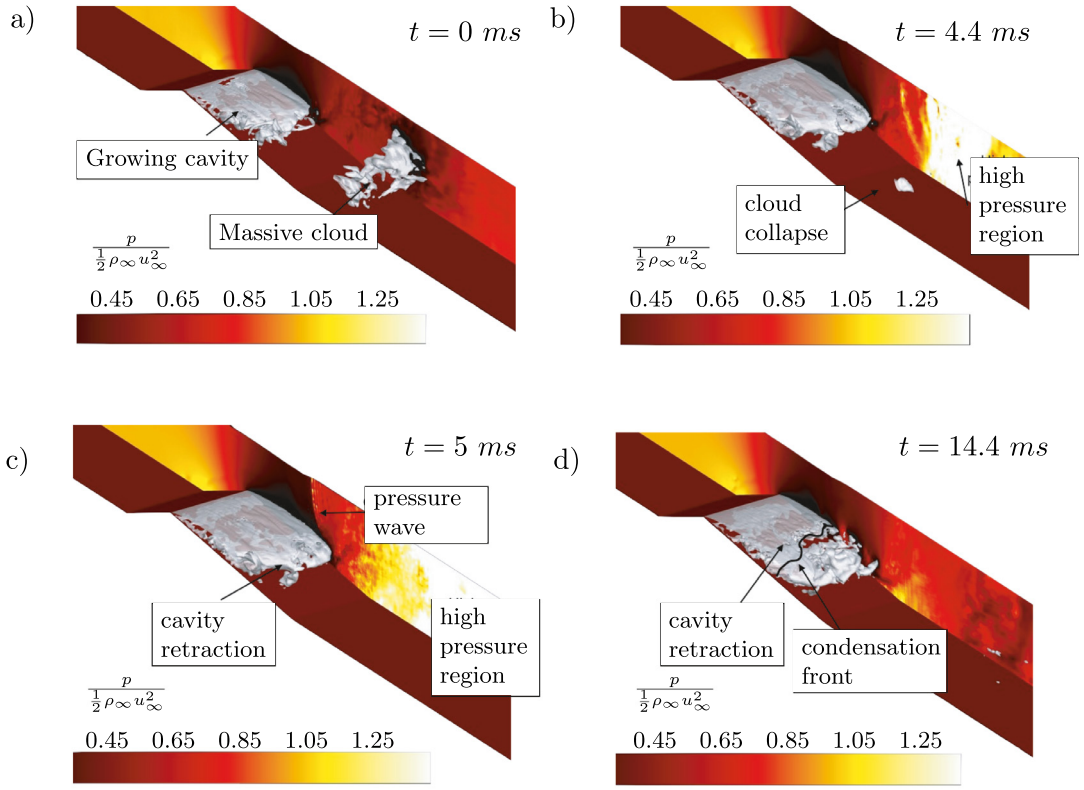

Fig. 18. Periodic shedding II: shedding cycle. Iso-contours level of $\alpha_v = 0.5$ with pressure plotted on side plane ($x - y$ plane at $z = 2.9h$). a) Growing cavity and previously shedded cloud ($t = 0$ ms), b) cloud collapse ($t = 4.4$ ms), c) collapse-induced pressure wave ($t = 5.0$ ms) and d) retracting cavity ($t = 14.4$ ms).

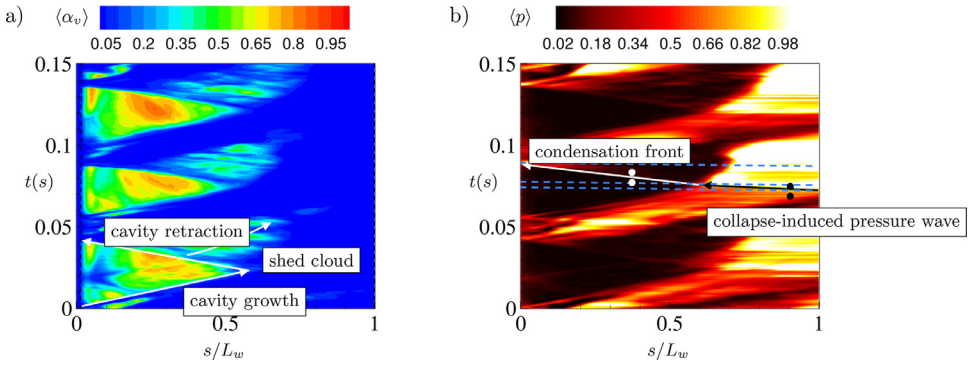

Fig. 19. Temporal evolution of spanwise averaged quantities taken on a line parallel to the wedge surface at a normal distance $n = 4$ mm for $0.15s$ showing approximately 3 cavity shedding cycles. a) $\langle\alpha\rangle$ and b) $\langle p\rangle$.

with pressure on the side plane as shown in Fig. 18. High pressure generated due to the collapse of large vapor clouds (visible in the Fig. 18(a)) is indicated in Fig. 18(b). Collapse-induced pressure waves impinging on the trailing edge of the cavity are visualized in Fig. 18(c). Note that Figs. 18(b) and (c) are only 0.6 ms apart. Subsequently, the retraction of the cavity by a condensation front is visualized in Fig. 18(d). The shedding cycle illustrates the cavity retraction due to the condensation front, initiated by the collapse-induced pressure wave from the previously shed cloud.

Time evolution over multiple cavity shedding cycles can be analyzed by constructing an $s - t$ diagram. We consider spanwise averaged quantities ($\langle\alpha_v\rangle$ and $\langle p\rangle$) along a line parallel to the wedge surface at a normal distance $n = 4$ mm, and stack them for multiple time instants as indicated in Fig. 19. The cavity is indicated by the triangular region. Cavity growth ($\sim t = 0.01$ s), cavity retraction ($\sim t = 0.03$ s) and shedding of the cloud is indicated by the arrow in Fig. 19(a) (cycles presented in the $s - t$ diagram are different from the instantaneous shedding cycle in Fig. 18). The cloud advects downstream as we march in time ($\sim t = 0.05$ s). Note that collapse of the cloud is not visible in the frame considered at $n = 4$ mm, rather it occurs at a higher normal distance and downstream of the wedge trailing edge. Fig. 19(b) visualizes the collapse-induced pressure wave impinging on the trailing edge of the cavity (indicated by black arrow $\sim\ t = 0.06$ s), and subsequent retraction of the cavity due to the propagation of condensation front (indicated by white arrow $\sim t = 0.06\text{s} - 0.08\text{s}$). Note the difference in the slopes of the collapse-induced pressure wave and the condensation front. The inverse of the slopes of the line indicate the speeds. As one would expect, the collapse-induced pressure wave travels much faster than the condensation front.

4.4.1. Rankine–Hugoniot jump conditions

Properties across the collapse-induced pressure wave and the condensation front are extracted at the points indicated in

Table 7
Properties ahead and behind of the collapse-induced pressure wave.

	p (kPa)	ρ (kg/m^3)	u_s (m/s)	Y	a (m/s)	S (m/s)	M_s
Pre-shock (L)	30.83	993.0	4.86	1.403×10^{-6}	74.54	−90.9	1.22
Post-shock (R)	66.92	997.0	4.29	9.215×10^{-7}	187.2		

Table 8
Properties ahead and behind of the condensation front.

	p (kPa)	ρ (kg/m^3)	u_s (m/s)	Y	a (m/s)	S (m/s)	M_s
Pre-shock (L)	2.23	172.9	−0.27	1.069×10^{-4}	3.88	−5.438	1.40
Post-shock (R)	5.248	973.7	−3.32	2.168×10^{-6}	15.74		

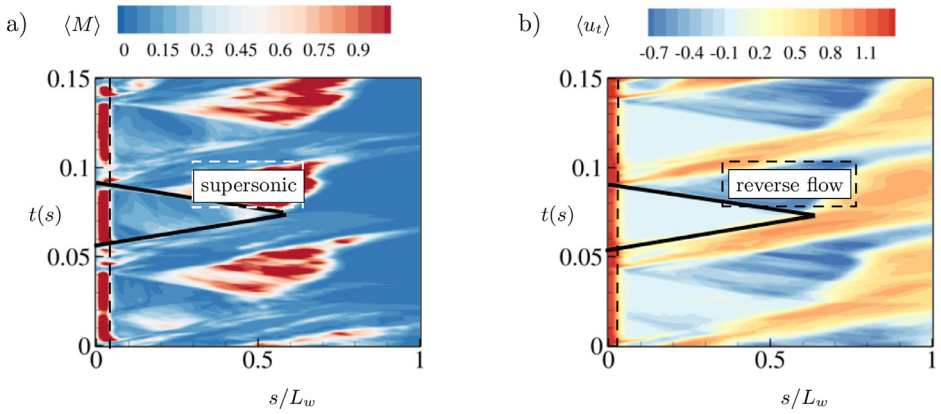

Fig. 20. Temporal evolution of spanwise averaged quantities taken on a line parallel to the wedge surface at a normal distance $n = 4$ mm for 0.15 s showing approximately 3 cavity shedding cycles. a) $\langle M \rangle$ and b) $\langle u_t \rangle$. Cavity is indicated by triangle shape formed by solid black line.

Fig. 19(b), and shown in Tables 7 and 8 respectively. Only a representative case is considered. Detailed derivation of Rankine-Hugoniot jump conditions for the current homogeneous mixture system is provided in Brandao et al., 2019. Expression for the shock speed as derived in Brandao et al., 2019 is given as:

$$S = u_L - \sqrt{\frac{(p_R - p_L)[\frac{p_R}{p_L}\frac{\overline{\gamma}_R+1}{\overline{\gamma}_R-1} + 1]}{(\rho_R - \rho_L)[\frac{p_R}{p_L} + \frac{\overline{\gamma}_L+1}{\overline{\gamma}_L-1}]}},$$
$$\frac{1}{\overline{\gamma}-1} = \frac{C_{vm}p + [C_{vm} + (1-Y_v)K_l]P_c}{[(Y_vR_v)(p+P_c) + (1-Y_v)K_l p]}. \quad (9)$$

Here, 'L' and 'R' respectively refer to the pre-shock and the post-shock states as shown in Tables 7 and 8. It is important to note that essentially both the collapse-induced pressure wave and the condensation front move through a bubbly mixture (not through a completely liquid phase of water). Collapse-induced pressure waves travel through a low void fraction bubbly mixture ($\sim$0.05) in the shed cloud, while the condensation front moves through extremely high volume fraction regions ($\sim$0.9) within the cavity. Shock speed obtained for the condensation front using Eq. (9), for the representative case chosen in Table 8, is −5.438 m/s. It is in close agreement with the mean value of the shock speed obtained from the slope of the $s-t$ diagram and experiments (see Table 4). Mach number based on the sound speed of 3.88 m/s ahead of the shock is 1.4, indicating the supersonic nature of the front. In addition, approximately two orders of magnitude jump in vapor mass fraction and an order of magnitude jump in density (see Table 8) indicate significant condensation of vapor as the front propagates. Accordingly, the front is referred as "condensation shock". A pressure ratio of 2.35 suggests that the condensation shock is a weak discontinuity in pressure (also observed by Ganesh et al. (2016) and Budich et al. (2018)). Interestingly, the velocity ahead of the shock (u_L) is only −0.29 m/s, which is less than an order of magnitude of the free stream velocity. As Eq. 9 suggests, u_L plays a critical role in determining the shock speed and consequently the nature of the condensation front.

For collapse-induced pressure waves, jumps in the vapor mass fraction and the density are very small. Speed of the pressure wave obtained from Eq. 9 is −90.9 m/s. Mach number based on the sound speed of 74.54 m/s ahead of the shock is 1.22; suggesting the supersonic nature of the pressure wave. This conclusion however is subject to some uncertainty due to cycle to cycle variations, probed location and accurate sound speed value in the low volume fraction bubbly mixture.

4.4.2. Cavity Mach numbers

We consider the time evolution of spanwise averaged Mach number ($\langle M \rangle$) and tangential velocity ($\langle u_t \rangle$) on a line parallel to the wedge at a normal distance $n = 4$ mm as indicated in Fig. 20. The cavity is illustrated by the black line. The region immediately following the cavity closure is indicated by a box; note that it is supersonic (Fig. 20(a)), and flow is reversed with a speed comparable to the free stream values (Fig. 20(b)). Interestingly, the cavity itself is subsonic despite the low speed of sound in the high volume fraction mixture (Fig. 20(a)). This is due to the negligible flow velocities within the cavity as shown in Fig. 20(b). This behavior is related to the vapor formation within the cavity in the periodic shedding case. In the periodic regime, it is observed that vapor is formed within the cavity during the cavity growth phase and upon formation it remains stationary.

5. Summary

LES is used to investigate partial cavitation over incipient, transitory and periodic regimes matching the experiments of Ganesh et al. (2016). LES captures both the re-entrant jet and the bubbly shock wave induced sheet to cloud transition in their respective regimes. Comparison to X-ray densitometry reveals that in the developed cavitation regimes, large regions of vapor in the

sheet/cloud and the resulting volume fraction field are accurately captured in the current simulations. In addition, instantaneous evolution of void fraction field, bubbly shock propagation speed and shedding frequency show very good comparison to the experiments.

Conditions favoring the formation of either the re-entrant jet or the bubbly shock wave are analyzed using LES. In the transitory regime, larger streamline curvature leads to higher adverse pressure gradient. This is observed both normal to the cavity and along the axial direction at the cavity closure. Higher adverse pressure gradient supports flow reversal and formation of re-entrant jet. The streamline curvature reduces with growing cavity moving from the transitory to the periodic regime. Reduction in the streamline curvature leads to smaller pressure recovery from within the cavity to outside. Hence, overall low pressures in the cavity closure lead to reduced speed of sound and increased medium compressibility. This favors the formation of shock waves in the periodic regime. In the re-entrant jet cycle, vapor production is observed predominantly in the shear layer and intermittently within the cavity. In the bubbly shock cycle, vapor production is observed over the entire thickness of cavity. With the reduction in σ_b, first the mean pressure inside the shear layer drops below vapor pressure. A further reduction in σ_b causes the mean pressure inside the cavity also to drop below vapor pressure along with the shear layer. This affects the vapor production and consequently the instability mechanisms.

Finally, in the periodic regime, bubbly shock waves are initiated by the collapse-induced pressure waves of the previously shed cloud. The process is illustrated using instantaneous plots and $s-t$ diagrams. The collapse-induced pressure wave travels through a highly compressible low volume fraction bubbly mixture. It subsequently impinges on the trailing edge of the cavity initiating the cavity retraction by a bubbly shock wave. Properties across collapse-induced pressure wave and the bubbly shock wave are analyzed using Rankine-Hugoniot jump conditions. Supersonic Mach numbers, significant condensation and smaller pressure rise are observed across the bubbly shock wave in accordance with the prior studies. Jumps in the vapor mass and density across the collapse-induced pressure waves are small. Interestingly, the regions within the cavity are subsonic despite low speed of sound due to extremely small velocities inside the cavity. Reverse flow and supersonic Mach numbers are observed in the cavity closure region.

Declaration of Competing Interest

The authors declare that they have no known competing financial interests or personal relationships that could have appeared to influence the work reported in this paper.

Acknowledgments

This work is supported by the United States Office of Naval Research under grants ONR N00014-14-1-0290 and ONR N00014-17-1-2676 with Dr. Ki-Han Kim as the program manager. The computations were made possible through the computing resources provided by Copper and Onyx of the High Performance Computing Modernization Program (HPCMP) and the Minnesota Supercomputing Institute (MSI). We acknowledge Dr. Harish Ganesh and Prof. Steve Ceccio at the University of Michigan, for providing the experimental data.

References

Arndt, R.E.A., Song, C.C.S., Kjeldsen, M., He, J., Keller, A., 2000. Instability of partial cavitation: a numerical/experimental approach. In: 23rd Symposium on Naval Hydrodynamics. National Academies Press, pp. 519–615.

Asnaghi, A., Bensow, R., Svennberg, U., 2017. Comparative analysis of tip vortex flow using RANS and LES. In: 7th International Conference on Computational Methods in Marine Engineering.

Bensow, R.E., Bark, G., 2010. Implicit LES predictions of the cavitating flow on a propeller. J. Fluids Eng. 132 (4), 1–10.

Bhatt, M., Gnanaskandan, A., Mahesh, K., 2015. Evaluation of finite rate homogenous mixture model in cavitation bubble collapse. 9th Int. Symp. Cavit..

Bhatt, M., Mahesh, K., 2018. Investigation of sheet to cloud transition due to the propagation of condensation fronts over a sharp wedge using large eddy simulations. 10th Int. Symp. Cavit..

Brandao, F.L., Bhatt, M., Mahesh, K., 2019. Numerical study of cavitation regimes in flow over a circular cylinder. J. Fluid Mech.. arXiv: 1911.03575

Budich, B., Schmidt, S., Adams, N., 2018. Numerical simulation and analysis of condensation shocks in cavitating flows. J. Fluid Mech. 838, 759–813.

Callenaere, M., Franc, J.-P., Michel, J., Riondet, M., 2001. The cavitation instability induced by the development of a re-entrant jet. J. Fluid Mech. 444, 223–256.

Coutier-Delgosha, O., Fortes-Patella, R., Reboud, J.-L., 2003. Evaluation of the turbulence model influence on the numerical simulations of unsteady cavitation. J. Fluids Eng. 125 (1), 38–45.

Eskilsson, C., Bensow, R., 2012. A compressible model for cavitating flow: comparison between Euler, RANS and LES simulations. 29th Symposium on Naval Hydrodynamics, Gothenburg, Sweden.

Foeth, E., Terwisga, T., Doorne, C., 2008. On the collapse structure of an attached cavity on a three-dimensional hydrofoil. J. Fluids Eng. 130, 71303.

Franc, J.-P., Michel, J.-M., 2005. Fundamentals of cavitation.

Frikha, S., Coutier-Delgosha, O., Astolfi, J.A., 2008. Influence of the cavitation model on the simulation of cloud cavitation on 2d foil section. Int. J. Rotating Mach. 2008.

Ganesh, H., Makiharju, S.A., Ceccio, S.L., 2016. Bubbly shock propagation as a mechanism for sheet-to-cloud transition of partial cavities. J. Fluid Mech. 802, 37–78.

Gnanaskandan, A., Mahesh, K., 2015. A numerical method to simulate turbulent cavitating flows. Int. J. Multiphase Flow 70, 22–34.

Gnanaskandan, A., Mahesh, K., 2016. Comparative study of RANS and LES in simulating cavitating flows. 31st Symposium on Naval Hydrodynamics. California, USA.

Gnanaskandan, A., Mahesh, K., 2016. Large eddy simulation of the transition from sheet to cloud cavitation over a wedge. Int. J. Multiphase Flow 83, 86–102.

Goncalves, E., Patella, R.-F., 2009. Numerical simulation of cavitating flows with homogeneous models. Comput. Fluids 38 (9), 1682–1696.

Gopalan, S., Katz, J., 2000. Flow structure and modeling issues in the closure region of attached cavitation. Phys. Fluids 12(4), 895–911.

Jahangir, S., Hogendoorn, W., Poelma, C., 2018. Dynamics of partial cavitation in an axisymmetric converging-diverging nozzle. Int. J. Multiphase Flow 106, 34–45.

Jakobsen, J.K., 1964. On the mechanism of head breakdown in cavitating inducers. J. Basic Eng. 291–305.

Kawanami, Y., Kato, H., Yamaguchi, H., Tanimura, M., Tagaya, Y., 1997. Mechanism and control of cloud cavitation. J. Fluids Eng. 119 (4), 788–794.

Kim, S., 2009. A numerical study of unsteady cavitation on a hydrofoil. In: 7th International Symposium on Cavitation, pp. 1–13.

Knapp, R.T., 1955. Recent investigations of the mechanics of cavitation and cavitation damage. ASME.

Laberteaux, K.R., Ceccio, S.L., 2001. Partial cavity flows. Part 1. Cavities forming on models without spanwise variation. J. Fluid Mech. 431, 1–41.

Long, Y., Long, X., Ji, B., Xing, T., 2019. Verification and validation of large eddy simulation of attached cavitating flow around a clark-y hydrofoil. Int. J. Multiphase Flow.

Makiharju, S.A., Ganesh, H., Ceccio, S.L., 2017. The dynamics of partial cavity formation, shedding and the influence of dissolved and injected non-condensable gas.. J. Fluid Mech. 829, 420–458.

Moin, P., Squires, K., Cabot, W., Lele, S., 1991. A dynamic subgrid-scale model for compressible turbulence and scalar transport. Phys. Fluids 3(11), 2746–2757.

Pendar, M.-R., Roohi, E., 2018. Cavitation characteristics around a sphere: an LES investigation. Int. J. Multiphase Flow 98, 1–23.

Peng, X., Ji, B., Cao, Y., Xu, L., Zhang, G., Luo, X., Long, X., 2016. Combined experimental observation and numerical simulation of the cloud cavitation with u–type flow structures on hydrofoils. Int. J. Multiphase Flow 79, 10–22.

Reisman, G.E., Wang, Y.C., Brennen, C.E., 1998. Observation of shock waves in cloud cavitation.. J. Fluid Mech. 355, 255–283.

Saito, Y., Takami, R., Nakamori, I., Ikohagi, T., 2007. Numerical analysis of unsteady behavior of cloud cavitation around a NACA0015 foil. Comput. Mech. 40, 85–96.

Schenke, S., van Terwisga, T.J., 2017. Simulating compressibility in cavitating flows with an incompressible mass transfer flow solver. In: 5th International Symposium on Marine Propulsors, Espoo, Finland, 1, pp. 71–79.

Schnerr, G.H., Sezal, I.H., Schmidt, S.J., 2008. Numerical investigation of three–dimensional cloud cavitation with special emphasis on collapse induced shock dynamics. Phys. Fluids 20 (4), 1–9.

Seo, J.H., Lele, S., 2009. Numerical investigation of cloud cavitation and cavitation noise on a hydrofoil section. In: 7th International Symposium on Cavitation, pp. 1–15.

Singhal, A.K., Athavale, M.M., Li, H., Jiang, Y., 2002. Mathematical basis and validation of the full cavitation model. J. Fluids Eng. 124 (3), 617–624.

Wang, Y., Wu, X., Huang, C., Wu, X., 2016. Unsteady characteristics of cloud cavitating flow near the free surface around an axisymmetric projectile. Int. J. Multiphase Flow 85, 48–56.

Wu, X., Maheux, E., Chahine, G.L., 2017. An experimental study of sheet to cloud cavitation. Exp. Therm Fluid Sci. 83, 129–140.